Spontaneous organization of columnar nanoparticles in Fe-BN nanocomposite films

D. Babonneau,* F. Pailloux, J.-P. Eymery, M.-F. Denanot, and Ph. Guérin
Laboratoire de Métallurgie Physique, UMR 6630 CNRS, Université de Poitiers, SP2MI, Téléport 2, Bvd M. et P. Curie, BP 30179, 86962 Futuroscope Chasseneuil Cedex, France

E. Fonda† and O. Lyon
Laboratoire pour l'Utilisation du Rayonnement Electromagnétique, Bât. 209D, Centre Universitaire, BP 34, 91898 Orsay Cedex, France
(Received 28 June 2004; revised manuscript received 14 September 2004; published 31 January 2005)

Ion-beam sputtering codeposition assisted with either reactive (nitrogen) or inert gas (neon, argon, and krypton) has been used to fabricate Fe-BN nanocomposite thin films of Fe-rich nanoparticles encapsulated in nanocrystalline boron nitride. A combination of high-resolution and conventional transmission electron microscopy (TEM), grazing incidence small-angle x-ray scattering (GISAXS), electron diffraction, x-ray absorption, and Mössbauer spectroscopy has been used to investigate the structural characteristics of these films, both at nanometric and atomic scales. Crystallized ε-Fe_3N nanoparticles (typically 2.5 nm in size) have been obtained in N assisted films, whereas self-organized arrays of amorphous Fe_2B nanocolumns ($\sim$3 nm in diameter and $\sim$10 nm in height, with small size dispersion) have been synthesized in inert-gas assisted films. Quantitative analysis of the GISAXS patterns and of the local autocorrelation functions of the TEM images indicate a better spatial ordering in the 50 eV Ar assisted films, i.e., when backscattering and sputtering effects are minimized. Our results shows that low-energy assistance with light ions can be used to control the morphology as well as the spatial ordering and chemical composition of nanoparticles in insulating matrix.

DOI: 10.1103/PhysRevB.71.035430 PACS number(s): 61.46.+w, 68.55.−a, 81.07.−b, 81.15.Cd

I. INTRODUCTION

Fe-based nanocomposite materials, in which nanoparticles are embedded in a nonmagnetic matrix (e.g., SiO_2, Al_2O_3, BN, C) have been extensively investigated because of their fundamental and technological interest.[1–10] To take advantage of their unique magnetic, electronic, optical, and transport properties in future nanoparticles-based devices, nanoparticles must be spatially ordered but also chemically and mechanically stable. Then it is important to control their chemical composition, their shape, their size, and size dispersion through elaboration process conditions. In recent years, nanocomposite films consisting of magnetic nanoparticles (e.g., Co, Fe, Ni, CoPt, FePt) encapsulated in graphitelike carbon have attracted much attention as possible candidates for high-density magnetic recording media, because graphite not only provides corrosion and wear resistance but also reduces interparticle exchange interactions.[9–14] In this context, encapsulation of magnetic nanoparticles in hexagonal boron nitride (*h*-BN, which crystallizes similar to graphite but is a good electrical insulator) may have significant advantages to control the spin-dependent tunneling between nanoparticles. Although disordered assemblies of *h*-BN nanocapsules containing iron oxide and cobalt oxide nanoparticles have already been obtained by arc melting methods,[15,16] most studies dealing with homogeneous *M*-BN nanocomposite films (with *M*=Fe, Co, CoPt, or FePt) reported metallic nanoparticles embedded in an amorphous phase of BN.[5–7,17,18] Nevertheless, we have recently demonstrated that Fe_2N nanoparticles encapsulated in *h*-BN can be produced by ion-beam sputtering codeposition assisted with a reactive nitrogen assistance beam.[8] In Ref. 8, the magnetic properties (saturation magnetization, coercitivity, blocking temperature) of unassisted and N assisted films were examined in detail.

In the present article we focus on the nanostructure of Fe-BN nanocomposite films grown by cosputtering under various assistance conditions. The influence of the nature of the assistance beam on the structural characteristics of the films, both at nanometric and atomic scales, is investigated in detail by complementary techniques. To study the spatial ordering of the nanoparticles and their morphology (shape, size, and size dispersion), we used transmission electron microscopy (TEM) and grazing incidence small-angle x-ray scattering (GISAXS) experiments. Chemical ordering of the nanoparticles (atomic composition and local environment) was examined by means of electron diffraction, extended x-ray absorption fine structure (EXAFS), and Mössbauer spectroscopy analyses.

The present article is organized as follows. Film fabrication details and deposition parameters are described in Sec. II. Nanometric scale characterizations (TEM and GISAXS results) are presented in Sec. III whereas the analysis of the local atomic order (electron diffraction, EXAFS, and Mössbauer measurements) is reported in Sec. IV. Finally, in Sec. V, a summary that discusses briefly the results and a conclusion are given.

II. SAMPLE FABRICATION

Fe-BN nanocomposite films were fabricated at 200 °C by ion-beam sputtering codeposition from a single target composed of a pure BN disk on which a high-purity Fe platelet (3 mm wide) was placed. The base pressure in the deposition chamber was 3×10^{-8} Torr and the sputtering process was carried out at 2×10^{-4} Torr by using a primary Ar^+ ion beam (energy 1.2 keV, current 80 mA). To obtain samples with various nanostructures, a secondary ion beam (energy

TABLE I. The experimental deposition conditions and the results from x-ray reflectometry analysis.

Sputtering beam (ion, energy)	Assistance beam (ion, energy)	Deposition time (min.)	Thickness (nm)	Critical angle[a] (°)
Argon, 1200 eV	No assistance	25	38.0±0.8	0.29±0.01
Argon, 1200 eV	Nitrogen, 50 eV	25	47.7±1.0	0.27±0.01
Argon, 1200 eV	Neon, 50 eV	25	36.6±0.8	0.30±0.01
Argon, 1200 eV	Argon, 50 eV	25	37.1±0.8	0.30±0.01
Argon, 1200 eV	Krypton, 50 eV	25	30.8±0.8	0.29±0.01

[a]With Cu-K_α radiation.

50 eV, current 40 mA) was employed to bombard the surface of the growing films with either reactive (nitrogen assistance) or inert (neon, argon, or krypton assistance) species. The films were deposited onto Si(001) substrates (covered with a native SiO_2 layer) for cross-sectional TEM observations, x-ray analyses, and Mössbauer measurements. Carbon-coated copper grids were used for plane-view TEM characterizations.

The thickness and critical angle for total external reflection of the unassisted and assisted films were determined by x-ray reflectometry using the Cu-K_α radiation. Table I summarizes the experimental conditions of deposition and the corresponding x-ray reflectometry results. It can be seen that, for a given deposition time of 25 min, most of the films have a thickness of about 37 nm and a critical angle of approximately 0.30°, corresponding to a Fe concentration of 26 at. %. It is, however, worth noting that the thickness of the Kr assisted film is 20% smaller, suggesting sputtering of the nanocomposite film by the Kr assistance beam. Moreover, it is observed that the reactive N assistance leads to a thickness 30% higher and a critical angle 10% smaller, as already described in Ref. 8. Let us point out that a set of thicker films (~200 nm, unassisted, N, Ne, and Ar assisted) was also fabricated for EXAFS and Mössbauer measurements.

III. MORPHOLOGY AND ORGANIZATION

A. TEM characterizations

Nanostructural characteristics of a series of Fe-BN films were investigated by high-resolution TEM (HRTEM) performed with a JEOL 3010 microscope (LaB_6, C_s=1.2 mm) operated at 300 keV. Figures 1(a)–1(c) are some representative plane view micrographs showing that the morphology of all the Fe-BN films is granular. The unassisted sample [Fig. 1(a)] consists of approximately 1.5-nm Fe-rich nanoparticles which are randomly distributed in an amorphous BN matrix with weak contrast. Furthermore, tilting of the sample in the microscope revealed no evident modification in the HRTEM image (not shown), indicating that the shape of the nanoparticles is quasispherical. By using an assistance beam during the growth of the films [Figs. 1(b) and 1(c)], the Fe-rich nanoparticles appear more contrasted and more regularly arranged within the matrix. Furthermore, their average size increases up to ~2.5 nm with Ne and ~3.5 nm with Ar assistance. The structure of the matrix is also progressively transformed into nanocrystalline BN. This is clearly observed in Fig. 1(c) that shows lattice fringes in the regions between the particles with a 0.3–0.4 nm spacing characteristics of the *h*-BN phase. A cross-sectional view of the Ar assisted film is presented in Fig. 1(d). The micrograph shows that the Fe-rich nanoparticles are uniformly elongated in the vertical direction. Furthermore (002) basal planes of the *h*-BN phase appear to be aligned along the growth direction, thus leading to observe Fe-rich nanocolumns encapsulated in poorly crystallized BN nanotubes. From these HRTEM experiments it can be seen that the use of a low-energy assistance beam is an effective way to act upon (i) the size of the nanoparticles, (ii) their shape, (iii) their local spatial ordering, and (iv) the crystalline structure of the matrix.

To describe more quantitatively the local spatial ordering of the Fe-rich particles with respect to the assistance conditions, image processing of bright-field TEM micrographs obtained with a conventional JEOL 200CX microscope was performed. We applied the method proposed by Fan and Cowley,[19] which is based on the analysis of local autocorrelation functions and which has been widely used in the past

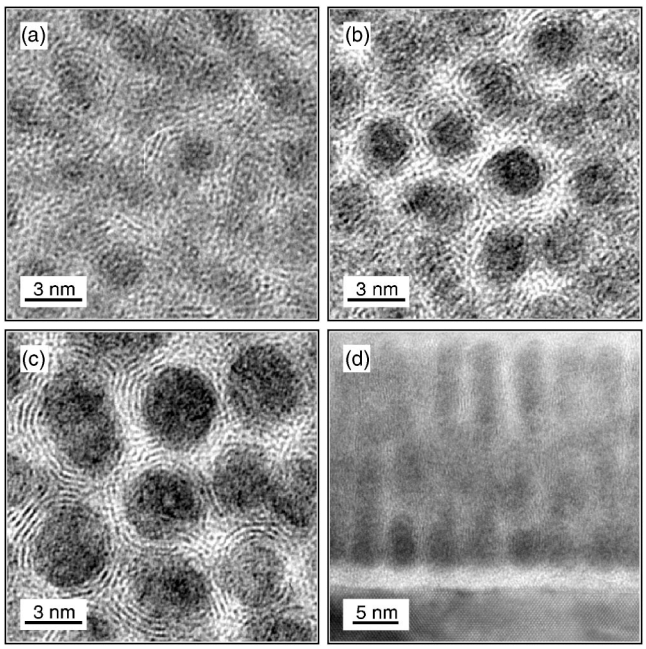

FIG. 1. HRTEM plane view micrographs of the (a) unassisted, (b) Ne-assisted, and (c) Ar-assisted Fe-BN films. (d) HRTEM cross-section micrograph of the Ar assisted Fe-BN film.

to investigate local chemical ordering in amorphous materials (see, for instance, Refs. 21 and 22). The main drawback of this technique is the limit imposed by the thickness of the sample, which may conceal the 3D ordering by the projection effect. In our case, the Fe-BN film thickness is not very large compared to the nanoparticle size, and the metal volume fraction is low so that we considered that the projection effects can be neglected, in particular in samples for which columnar growth occured. A typical low-magnification TEM plane view micrograph of our Fe-BN films is presented in Fig. 2(a). It shows dark dots (the Fe-rich nanoparticles) distributed over a bright background (the BN matrix). As seen in Fig. 2(b), the autocorrelation function (ACF) of such an image, calculated over a large area of the order of 0.4 μm^2, is radially symmetric. This indicates that, at this observation scale, the probability of finding a neighbor particle at the distance R (R is the radius of the main ring in the ACF) from a central particle is the same in all directions. Hence, it is concluded that there is no long-range ordering between the Fe-rich nanoparticles. In contrast, Fig. 2(c) clearly shows that the local autocorrelation function (LACF) calculated over a smaller area of a few hundred nm^2 presents fringes and even dots, which evidence short-range ordering in specific directions. Obviously, the fringes or dot patterns exhibit different orientations from one small area of the image to another, so that the sum of a large number of LACFs shows no more information than the ACF of the whole image. The method proposed by Fan and Cowley[19] consists in rotating all the LACFs to reach the best match between each LACF and a reference one, arbitrary chosen. Hence, the sum of the rotated LACFs provides an image of the most representative pattern present in the whole image if one exists (otherwise the sum remains radially symmetric). We give in the following a brief description of the algorithm that we have used to analyze the obtained TEM images.

(1) TEM plane view images of the Fe-BN films were first digitized (256 gray levels) and the sampling was tuned so that the mean distance between particles expressed in pixel (px) units remains the same for each image of each sample (we decided to set this value at 10 px). This ensures that the number of particles involved in the processing is roughly the same ($\sim 10^4$), whatever the sample.

(2) 1024×1024 px^2 images were then divided into small cells (64×64 px^2 or 128×128 px^2). The scaling of the cells is one of the ways to check the extent of the ordering. To avoid the well known "wrap-around" artifact during the fast Fourier transform process, each cell was first embedded in a larger image filled with the mean value of the intensity of this cell.

(3) As the choice of the reference cell is arbitrary, we chose to use the same reference pattern for all the samples in order to compare samples together. The cells were then extracted from the experimental images and their ACFs were compared and rotated (1° step) with respect to the ACF of the reference cell to reach the best correlation parameter as determined by the Pearson correlation coefficient.[20]

(4) The rotated LACFs were then summed to get a picture of the main feature in the images. If local ordering occurs, specific symmetries should be observed in this averaged sum of the rotated LACFs [Fig. 3(a)] as well as high radial and circular contrasts [Figs. 3(b) and 3(c)].

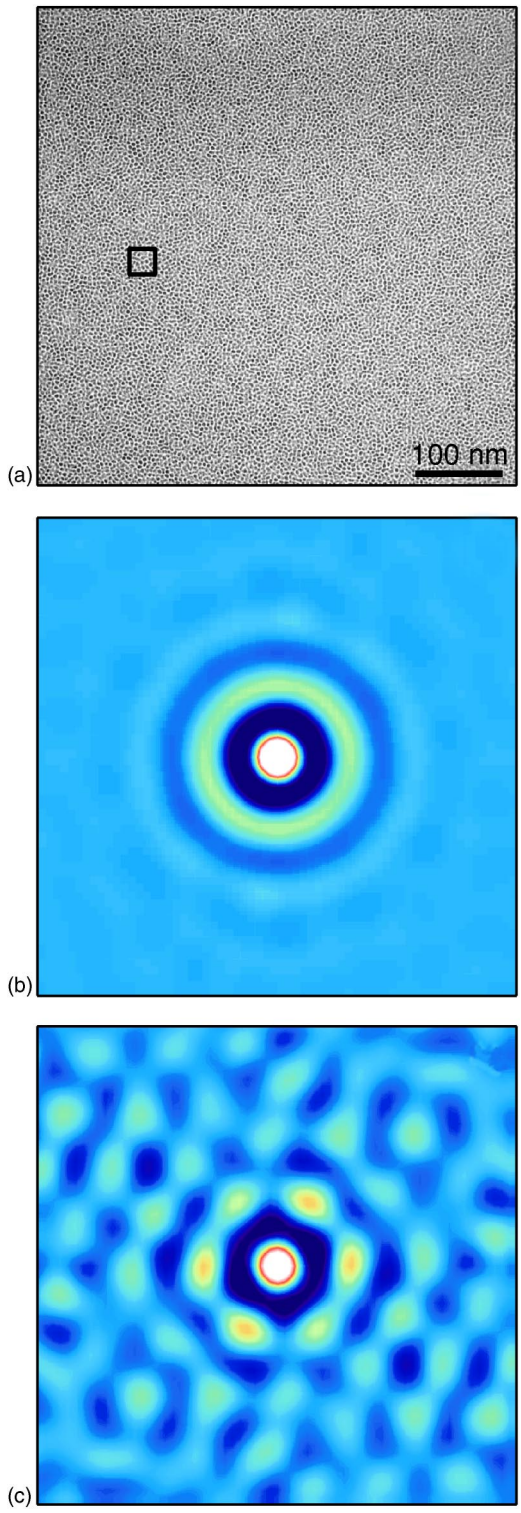

FIG. 2. (Color online) (a) 1024×1024 px^2 TEM plane view micrograph of the Ar-assisted Fe-BN film. (b) Central area of the autocorrelation function (ACF) in Fig. 2(a); the radial symmetry of the ACF indicates that all the directions are equivalent at this observation scale. (c) ACF of the 64×64 px^2 area delimited by the black square in Fig. 2(a); the presence of both fringes and dots evidences short-range ordering for the Fe-rich particles.

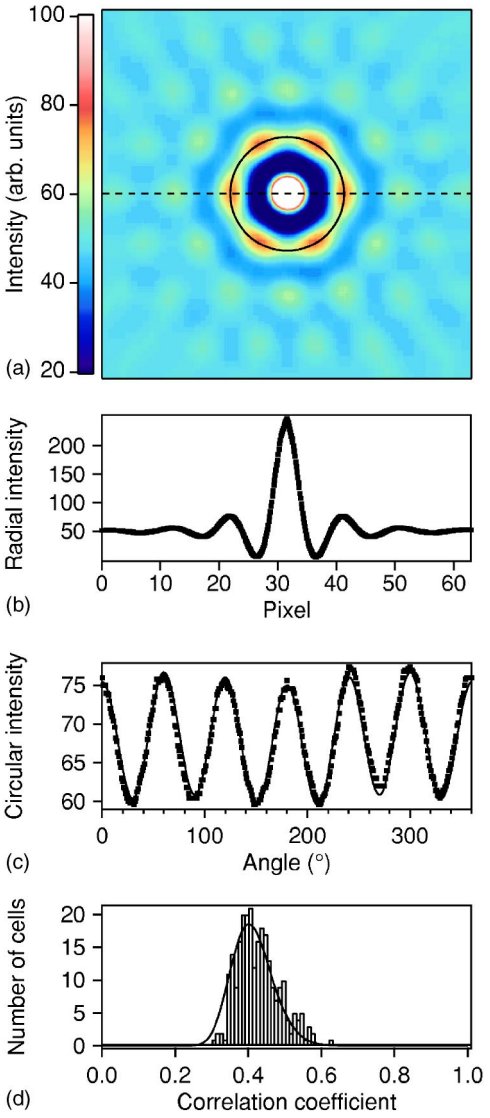

FIG. 3. (Color online) (a) Averaged sum of the rotated local autocorrelation functions of the Ar-assisted film using 64×64 px^2 cells (hexagonal reference). (b) Variation of the intensity along the dotted line in Fig. 3(a) that enables the radial contrast to be determined as the amplitude of the first secondary maximum normalized over the background. (c) Variation of the intensity along the solid line in Fig. 3(a) that enables the circular contrast to be determined as the amplitude of the signal. (d) Histogram of correlation coefficients fitted to a log-normal distribution.

(5) The histograms of correlation coefficients were also plotted and fitted with a log-normal distribution [Fig. 3(d)]. In the case of local ordering similar to that of the reference pattern, the histogram should be quite sharp and the correlation coefficient at the maximum of the distribution should reach a high value.

The process described above was applied to compare the local spatial ordering in Fe-BN nanocomposite films depending on the nature of the assistance ion beam. Although it seems obvious from direct observation of the LACFs that the hexagonal ordering is the most likely, we carried out the analysis with two kinds of reference pattern: a square pattern and a hexagonal one. As suspected, the results obtained for the hexagonal reference are better than those obtained for the square pattern, except for the N assisted and unassisted films for which they were of the same quality. Results obtained for the hexagonal reference using 64×64 px^2 cells are summarized in Table II. Whatever the ordering criterion we consider (symmetry properties and contrast in the averaged sum of the rotated LACFs, width, and maximum of the correlation coefficient distribution), it shows that the greatest extent of local ordering is obtained for the Ar assisted film. Although slightly lowered, the ordering extent remains excellent for the Ne assisted film and it decreases again for the Kr assisted film. In contrast, the ordering in the N assisted and unassisted samples is very limited (it vanishes after three consecutive neighbors) as shown by the weak contrast in the averaged sum of the rotated LACFs and the low values of the correlation coefficients. It is also worth noting that these results are confirmed by the analysis performed using 128×128 px^2 cells. Hexagonal symmetry is still observed in the averaged sum of the rotated LACFs of the Ar assisted film, indicating that in-plane ordering statistically remains up to five consecutive neighbors [Fig. 4(a)], whereas a radially symmetric pattern is obtained for the unassisted film [Fig. 4(b)].

TABLE II. The results obtained from the analysis of the local autocorrelation functions (LACF's) of the bright-field TEM plane view micrographs using 64×64 px^2 cells (hexagonal reference).

Sample	Radial contrast[a]	Circular contrast[b]	Maximum of the distribution[c]	FWHM of the distribution[d]
Unassisted	0.40	5.16	0.331	0.135
N assisted	0.26	3.92	0.320	0.107
Ne assisted	0.46	7.96	0.392	0.136
Ar assisted	0.52	7.91	0.404	0.128
Ar assisted[e]	0.42	0.20	0.263	0.195
Kr assisted	0.42	7.78	0.379	0.139

[a]Determined from the averaged sum of the rotated LACF's [see Fig. 3(b)].
[b]Determined from the averaged sum of the rotated LACF's [see Fig. 3(c)].
[c]Determined from the histogram of correlation coefficient [see Fig. 3(d)].
[d]Determined from the histogram of correlation coefficient [see Fig. 3(d)].
[e]The LACF's were not rotated in this case for comparison.

B. GISAXS experiments

GISAXS measurements were performed with the aim of getting accurate morphological characteristics (i.e., shape, lateral and vertical sizes, size dispersion) of the Fe-rich particles depending on the assistance conditions, but also to check the spatial ordering over a large sample area of the order of 15 mm^2. GISAXS experiments were carried out with the small-angle scattering setup of beamline DW31B at the LURE synchrotron facility (Orsay, France). The lateral and vertical beam sizes were 1 and 0.1 mm, respectively, and the wavelength was $\lambda=0.177$ nm. The angle of incidence

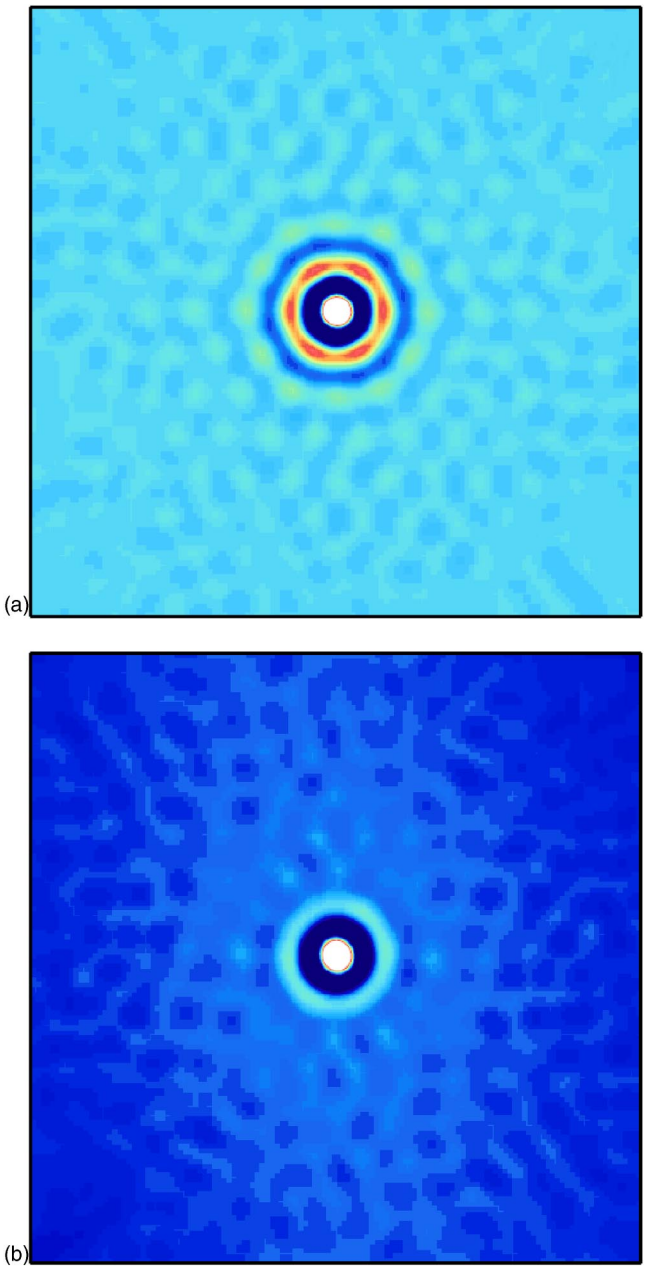

FIG. 4. (Color online) Averaged sum of the rotated local autocorrelation functions of the (a) Ar- and (b) N-assisted films using 128×128 px^2 cells (hexagonal reference); specific symmetries can be seen in Fig. 4(a), indicating a high degree of ordering for the Fe-rich particles in the Ar-assisted film.

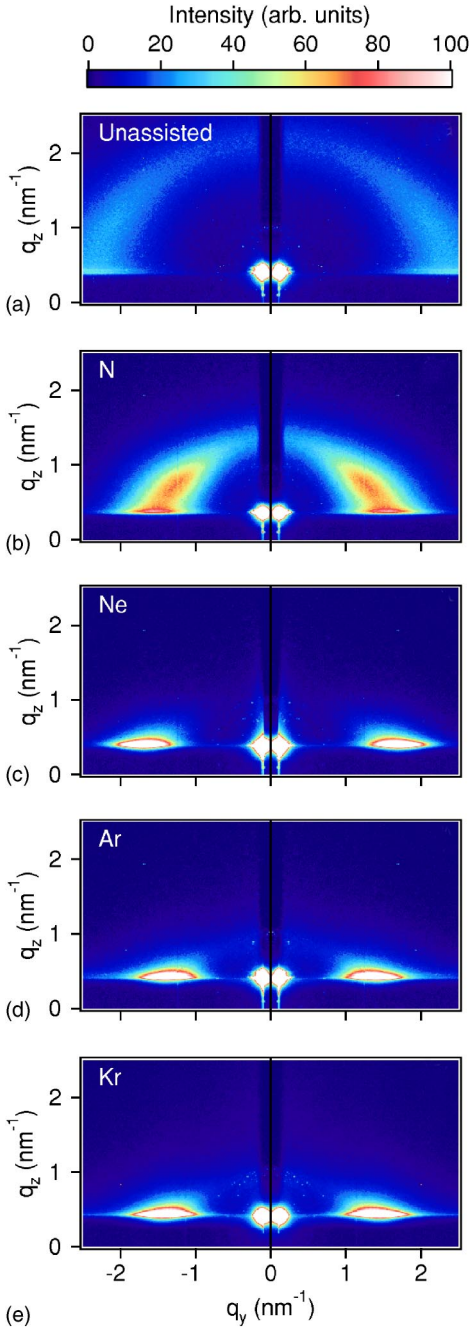

FIG. 5. (Color online) 2D experimental GISAXS patterns of Fe-BN nanocomposite films: (a) unassisted, (b) N assisted, (c) Ne assisted, (d) Ar assisted, and (e) Kr assisted.

with respect to the surface (α_i) was kept slightly above the critical angle of total external reflection (α_c), so that the penetration depth of the incident x-ray beam was of the order of the film thickness. The transmitted and specularly reflected beams were masked by a vertical beam stop, and the scattered intensity originating from typically 10^{12} particles was collected with a CCD detector placed at 380 mm from the sample. 2D experimental GISAXS patterns of Fe-BN films grown with various assistance conditions are displayed in Figs. 5(a)–5(e) where the horizontal and vertical components of the scattering vector in vacuum $\mathbf{q}=(q_y,q_z)$ (the q_x coordinate always remains negligible) were calculated as[23]

$$\mathbf{q} = \frac{2\pi}{\lambda}[(\sin(2\theta_f)\cos(\alpha_f)\ ,\sin(\alpha_f) + \sin(\alpha_i)] \qquad (1)$$

with $2\theta_f$ and α_f being the exit angles with respect to the incidence plane and the surface plane, respectively. A visual inspection of the 2D experimental GISAXS patterns provides a first qualitative information about the morphology of the Fe-rich particles. The 2D GISAXS patterns for the unassisted and N assisted films [Figs. 5(a) and 5(b)] exhibit elliptic

TABLE III. The results obtained from the analysis of the 2D experimental GISAXS patterns with the local monodisperse hard-sphere model. Expressions for the form factor $F(\tilde{q})$ (cylinder, spheroid, or capsule) and values for the out-of-plane volume fraction of the hard spheres $\eta_{HS}^{\perp}$ ($\eta_{HS}^{\parallel}$ or 0) are those yielding the best fits within the approximations given in the text.

Sample	$F(\tilde{q})$	$D^{\parallel}$ (nm)	$w^{\parallel}$ (nm)	$D^{\perp}$ (nm)	$C^{\parallel,\perp}$	$\eta_{HS}^{\parallel}$	$\eta_{HS}^{\perp}$
Unassisted	spheroid	1.69	0.76	2.00	1.316	0.396	$\eta_{HS}^{\parallel}$
N assisted	spheroid	2.51	1.20	3.26	1.354	0.392	$\eta_{HS}^{\parallel}$
Ne assisted	capsule	2.71	0.76	9.11	1.417	0.513	0
Ar assisted	capsule	3.46	1.55	9.20	1.244	0.539	0
Kr assisted	capsule	2.61	0.56	8.56	1.725	0.424	0

scattering rings characteristic of a 3D arrangement of nanoparticles slightly elongated in the vertical direction.[24] In contrast, the 2D GISAXS patterns for the Ne, Ar, and Kr assisted films [Figs. 5(c)–5(e)] display a very anisotropic signal, indicating a columnar growth of the Fe-rich nanoparticles consistent with the HRTEM results. To provide quantitative information on the nanoparticle shape and spatial arrangement, a detailed analysis of the GISAXS intensity is then necessary. In the framework of the distorted-wave Born approximation, the scattered intensity originating from a system of monodisperse particles buried in a thin layer is given by[25]

$$I(\mathbf{q}) = k|T(\alpha_i)|^2|T(\alpha_f)|^2|F(\tilde{\mathbf{q}})|^2 S(\tilde{\mathbf{q}}), \tag{2}$$

where $\tilde{\mathbf{q}}=(\tilde{q_y},\tilde{q_z})$ is the complex scattering vector in the layer (corrected for refraction at the air/layer interface and for absorption in the layer), k is an overall scale factor, $T(\alpha_i)$ and $T(\alpha_f)$ are the Fresnel transmission coefficients in incidence and emergence, $F(\tilde{\mathbf{q}})$ is the form factor of the scattering objets (Fourier transform of the particle shape), and $S(\tilde{\mathbf{q}})$ is the structure factor of the assembly, which represents the interparticle interference function. It should be noted that reflections of the incident and scattered beams at the layer/substrate interface are neglected as the penetration depth is low. Assuming that all particles are surrounded by particles of identical size, the local monodisperse approximation (LMA) is commonly used to include the polydispersity of the system in the model.[26] In our case, this assumption is supported by the TEM images of the Fe-BN films where particles of very different sizes close to one another are not observed. The polydisperse system is thus considered as the sum of monodisperse subsystems weighted by the size distribution. Hence, the scattered intensity can be expressed as[27,28]

$$I_{LMA}(\mathbf{q}) = \int_0^{\infty} I(\mathbf{q}) N(D) dD, \tag{3}$$

where $I(\mathbf{q})$ is given by Eq. (2) and $N(D)$ represents the distribution of particle size that was taken as a Gaussian function of full width at half maximum (FWHM) w. In our model, three possible shapes for the Fe-rich particles of in-plane diameter $D^{\parallel}$ and height $D^{\perp}$ were tested, namely, cylinder, oblate spheroid (rotational ellipsoid elongated along the vertical direction), and capsule (cylinder of diameter $D^{\parallel}$ and height $D^{\perp}-D^{\parallel}$ with one hemisphere of diameter $D^{\parallel}$ at each tip), whose mathematical expressions for the form factor $F(\tilde{\mathbf{q}})$ are given in Appendix A. The model also includes the structure factor $S(\tilde{\mathbf{q}})$ expressed within the Percus-Yevick approximation for monodisperse hard spheres[29] and depicted in Appendix B. The expression for $S(\tilde{\mathbf{q}})$ depends on the volume fraction η_{HS} of the hard spheres, which is characteristic of the local spatial ordering; $S(\tilde{\mathbf{q}})$ also depends on the hard-sphere diameter D_{HS} which is considered to be proportional to the particle size through a constant factor C, assuming the Fe-rich particles to be surrounded by a depleted zone which volume is proportional to the volume of the particles.[30] To deduce the in-plane and out-of-plane particle shape parameters ($D^{\parallel,\perp}$ and $w^{\parallel,\perp}$) and the spatial correlation parameters ($C^{\parallel,\perp}$ and $\eta_{HS}^{\parallel,\perp}$) from the 2D experimental GISAXS patterns presented in Figs. 5(a)–5(e), two cuts of the intensity map were simultaneously fitted. The first cut was performed parallel to q_y at $q_z \approx 0.43$ nm^{-1} corresponding to the minimum q_z value $q_z^{min}=(2\pi/\lambda)[\sin(\alpha_c)+\sin(\alpha_i)]$ as deduced from Eq. (1). The second cut was achieved parallel to q_z, either at $q_y = q_z^{min}$ (unassisted and N assisted films) or at the q_y position of the interference maximum in the first cut (Ne, Ar, and Kr assisted films). The Levenberg-Marquardt algorithm[31] was used to search for the parameter values minimizing χ^2 for both cuts. However, to limit the number of fitting parameters, two crude approximations were made: (i) $w^{\perp}/w^{\parallel}=D^{\perp}/D^{\parallel}$ (i.e., all the particles of the population have the same aspect ratio) and (ii) $C^{\perp}=C^{\parallel}$ and $\eta_{HS}^{\perp}=\eta_{HS}^{\parallel}$ (i.e., 3D particle distribution with in-plane and out-of-plane spatial correlation described by the same parameters) or $\eta_{HS}^{\perp}=0$ [i.e., 2D particle distribution without out-of-plane spatial correlation leading to $S(\tilde{q_z})=1$]. 2D simulated GISAXS patterns were then calculated with the parameters obtained from the fits and reported in Table III. χ^2 maps were finally plotted, with χ^2 defined as $\chi^2(q_y,q_z)=[I_{exp}(q_y,q_z)-I_{sim}(q_y,q_z)]^2/I_{sim}(q_y,q_z)$.

As an example, Fig. 6 shows that a good agreement between the simulated and experimental data is obtained for the unassisted film by assuming spheroidal (quasispherical) particles and $\eta_{HS}^{\perp}=\eta_{HS}^{\parallel}$ in the model. Identically, a 3D distribution of oblate spheroids allows one to reproduce the 2D experimental pattern of the N-assisted film over the whole q range. In contrast, as seen in Fig. 7 corresponding to the analysis of the Ar assisted film, the best reproduction of the 2D experimental patterns for the films assisted with inert gas is obtained by assuming vertically elongated capsules and $\eta_{HS}^{\perp}=0$. In this case however, it should be noted that the

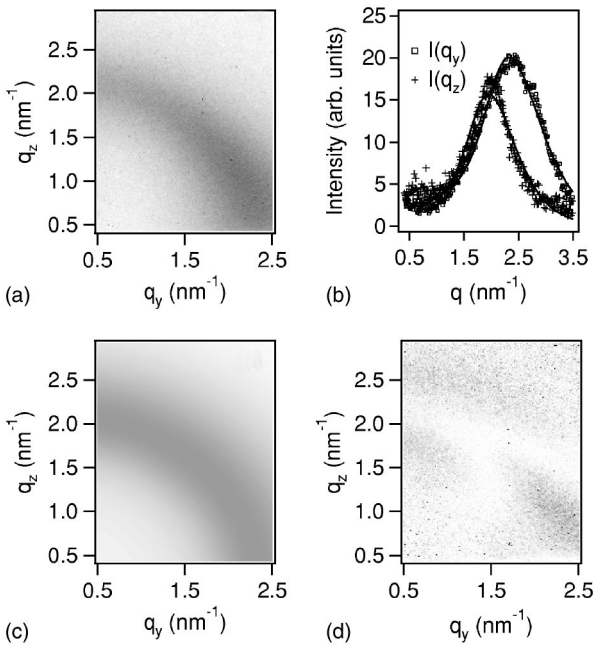

FIG. 6. (a) 2D experimental GISAXS pattern of the unassisted Fe-BN film. (b) Cuts of the experimental pattern parallel to q_y at $q_z=0.43$ nm^{-1} and parallel to q_z at $q_y=0.43$ cm^{-1}; best fits of the experimental cuts (solid lines). (c) 2D simulated GISAXS pattern with the parameters gathered in Table III. (d) χ^2 map with $\chi^2(q_y,q_z)=[I_{\mathrm{exp}}(q_y,q_z)-I_{\mathrm{sim}}(q_y,q_z)]^2/I_{\mathrm{sim}}(q_y,q_z)$.

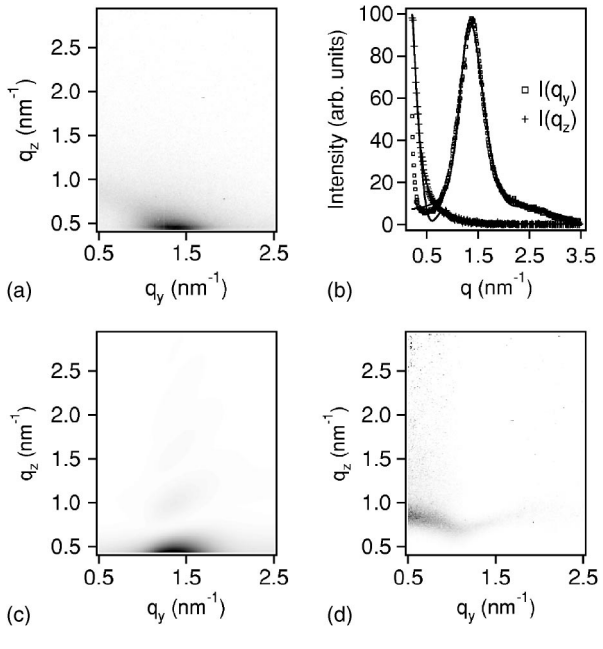

FIG. 7. (a) 2D experimental GISAXS pattern of the Ar-assisted Fe-BN film. (b) Cuts of the experimental pattern parallel to q_y at $q_z=0.43$ nm^{-1} and parallel to q_z at $q_y=1.36$ nm^{-1}; best fits of the experimental cuts (solid lines). (c) 2D simulated GISAXS pattern with the parameters gathered in Table III. (d) χ^2 map with $\chi^2(q_y,q_z)=[I_{\mathrm{exp}}(q_y,q_z)-I_{\mathrm{sim}}(q_y,q_z)]^2/I_{\mathrm{sim}}(q_y,q_z)$.

simulated data in the direction parallel to q_z display oscillations that are not present in the corresponding experimental data [Fig. 7(b)]. We attribute this discrepancy to a particle height distribution broader than the in-plane diameter one ($w^{\perp}>w^{\parallel}$), as seen in the cross-section HRTEM image of the same sample [Fig. 1(d)]. Furthermore, whereas the χ^2 map of the unassisted film in Fig. 6(d) is rather flat, the χ^2 map of the Ar assisted film in Fig. 7(d) exhibits a stronger signal at low q_y values for $q_z\approx 0.8$ nm^{-1}, owing to the vertical spatial correlations (even weak) that are not taken into account in the 2D distribution model.

In summary, according to the GISAXS results reported in Table III, the use of a low-energy assistance beam during the ion-beam sputtering deposition of granular Fe-BN films leads to dramatic changes in morphology and spatial ordering of the Fe-rich particles, especially when inert gas are used. In comparison with the unassisted film, we observe an increase of the average in-plane particle diameter $D^{\parallel}$ (from 1.69 nm to a maximum value of 3.46 nm for Ar), a narrowing of the in-plane size distribution $w^{\parallel}/D^{\parallel}$ (from $\sim$50% to $\sim$30%), and an increase of the aspect ratio $D^{\perp}/D^{\parallel}$ (from $\sim$1.2 to $\sim$3). These morphological modifications are accompanied by a decrease of the out-of-plane hard-sphere volume fraction $\eta_{\mathrm{HS}}^{\perp}$ (corresponding to a transition from a 3D particle distribution to a 2D one) and an increase of the in-plane hard-sphere volume fraction $\eta_{\mathrm{HS}}^{\parallel}$. It corroborates the analysis of the TEM images, which indicates a better in-plane spatial ordering in the Ar and Ne assisted films than in the other films.

IV. LOCAL ATOMIC ORDER

A. Electron diffraction results

Being complementary to bright-field TEM experiments, electron diffraction was used to provide information about the crystalline nature of the Fe-BN films. As typical examples, selected-area electron diffraction (SAED) patterns of the Ar- and N-assisted films are shown in Figs. 8(a) and 8(b). In both cases, all the spectral rings are broad due to crystalline domains with small size and/or disordered structure. The diffraction profiles of the unassisted (dotted line) and assisted films (solid lines) were extracted from the corresponding SAED patterns and are displayed in Fig. 8(c) together with the position of the main lines for α-Fe (circles), ε-$Fe_{2-3}N$ (down triangles), Fe_2B (up triangles), and *h*-BN (vertical line).[32] The first peak corresponding to the innermost halo ring in the SAED patterns arises from the BN matrix and confirms the presence of nanocrystalline *h*-BN in all the assisted films (the peak is weaker and broader for the unassisted film because of the amorphous structure of the BN matrix). A corresponding *d* spacing of approximately 0.36 nm is estimated, slightly higher than that of the (002) basal planes in bulk *h*-BN, $d_{002}=0.33$ nm, as already observed in Fe-BN and Fe-C nanocomposite films.[6,10] The main feature in Fig. 8(c) is that the inert-gas assisted films have the same characteristics as the unassisted film with two broad peaks indexed as α-Fe(B) or Fe_2B (even the presence of FeB or Fe_3B phases cannot be ruled out due to the overlapping of the spectral lines). Only the N assisted film exhibits a different profile, which reveals the presence of ε-$Fe_{2-3}N$ indicating that nitrided Fe particles are formed in this case.

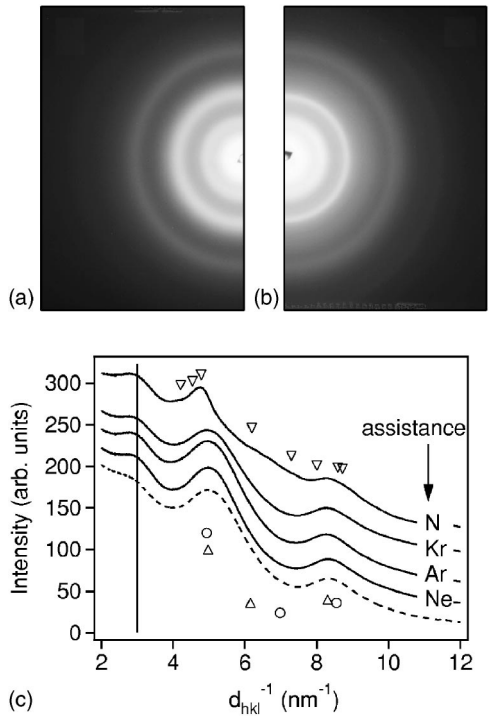

FIG. 8. SAED patterns of the (a) Ar- and (b) N-assisted Fe-BN films. (c) Electron diffraction averaged profiles obtained from the SAED pattern of the unassisted (dotted line) and assisted (solid lines) Fe-BN films together with the position of the main lines for α-Fe (circles), ε-$Fe_{2-3}N$ (down triangles), Fe_2B (up triangles), and *h*-BN (vertical line).

B. EXAFS analysis

From SAED characterizations, it was evidenced that the nanoparticles embedded in BN are not pure α-Fe particles whatever the assistance conditions. Unfortunately, it is tricky to determine the exact crystalline structure of the particles by electron diffraction experiments, in particular because of the line broadening resulting from small grain sizes and/or crystalline disorder. Accordingly, EXAFS measurements were performed in the total electron yield mode at the LURE synchrotron facility on beamline D42 operating with a Si(111) channel cut monochromator. The intensity of the monochromatic beam was monitored by an air filled ionization chamber, while the absorption coefficient of the Fe-BN films was recorded in conversion electron yield at liquid nitrogen temperature,[33] with the probed depth being in the 100 nm range,[34,35] thus of the order of magnitude of the thickness of the studied films (~200 nm). The samples, electrically connected to ground, were introduced in a chamber continuously flushed by He and were positioned at about 20° with respect to the incoming beam. He gas passed through a liquid nitrogen filled Dewar before entering the measurement chamber, and it was therefore used to cool the sample. For a complete description of this method, Refs. 36 and 37 can be consulted. EXAFS spectra were obtained from absorption data by the AUTOBK 2.941 code.[38] Data analysis has been performed with FEFFIT 2.984 (Ref. 39) versus theoretical standards obtained with FEFF 8.1 self-consistent calculations.[40] Data fitting was performed in *r* space on k^2-weighted spectra, but

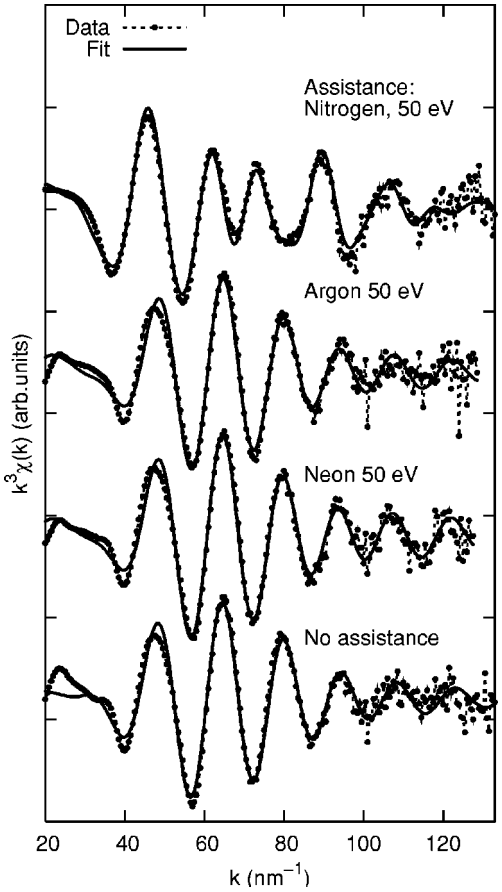

FIG. 9. The k^3-weighted EXAFS spectra of Fe-BN nanocomposite films prepared with different assistance conditions.

k^3-weighted EXAFS are shown in Fig. 9 to better visualize the structure in the high *k* range. A difference between the N assisted film and the others is evident from a visual inspection of the EXAFS signals as shown in Fig. 9 and their Fourier transforms presented in Fig. 10.

Quantitative analysis of the unassisted, Ne-assisted, and Ar-assisted films evidences the relatively disordered nature of the structure. Local structure around Fe can be simply simulated by Fe-B and Fe-Fe contributions. From the results listed in Table IV, it can be seen that the Fe-B distance (0.206 nm) is significantly shorter than in FeB (0.212 nm), while the Fe-Fe distance (0.249 nm) corresponds well to that in α-Fe metal (0.248 nm). Small coordination numbers of Fe-B and Fe-Fe distances suggest the formation of small particles, most likely including a large amount of B in the form of a $Fe_{100-x}B_x$ amorphous phase.

The N assisted film has a more defined local structure with more apparent shells and their few relative multiple scattering paths have been introduced in the refinement. Results are also depicted in Table IV. The first distance is too short to be related to a B shell and it can be well reproduced as a Fe-N shell at 0.192 nm as can be found in ε-Fe_3N. Outer shells are quite disordered but three distinct Fe-Fe distances can be observed: 4×0.260, 2×0.278, 4×0.388 nm. They do not correspond exactly to the local structure in ε-Fe_3N: 6×0.267, 6×0.273, 2×0.378, 4×0.384 nm, but their likelihood suggests that the formed

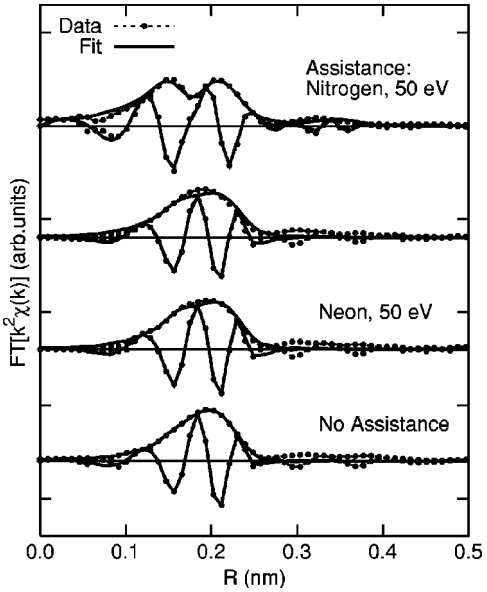

FIG. 10. Fourier transform (imaginary part and modulus) of the k^2-weighted EXAFS spectra of Fe-BN nanocomposite films prepared with different assistance conditions.

compound is quite similar, this compound can be the result of the direct reaction of Fe with the assistance nitrogen beam.

C. Mössbauer measurements

^{57}Fe Mössbauer measurements were undertaken to investigate the Fe atom environments and then obtain further information on the Fe-rich phases. Conversion electron Mössbauer spectroscopy (CEMS) experiments were performed at room temperature by using a constant-acceleration setup in reflection geometry, with a ^{57}Co source diffused into a rhodium matrix (1.85 GBq). A He-CH_4 gas flow proportional counter[41] was used to record the emitted conversion (7.3 keV) and Auger (5.5 keV) electrons subsequent to the resonant γ-ray scattering by ^{57}Fe nuclei. The isomer shift (IS) at the ^{57}Fe nucleus is given relative to α-Fe at room temperature. As is known, the CEMS technique is well suited for surface and thin film studies, since it is most sensitive to the top (~100 nm) of the sample (nearly 80% of conversion electrons come from this depth), even though there is some contribution to the signal from a depth up to ~250 nm, but with decreasing efficiency.[42]

TABLE IV. The results obtained from the analysis of EXAFS spectra: type and number of nearest neighbors, corresponding distance and Debye-Waller factor σ^2, giving the mean square relative displacement.

Sample	Shell	Type of neighbor	Coordination number	Distance (nm)	σ^2 (10^{-4} nm^2)
Unassisted	1	B	3(1)	0.206(2)	0.9(4)
	2	Fe	4.7(7)	0.249(1)	1.3(1)
Ne assisted	1	B	2.6(7)	0.205(2)	0.6(2)
	2	Fe	3.9(5)	0.249(1)	1.1(1)
Ar assisted	1	B	3(1)	0.206(2)	0.8(4)
	2	Fe	4.2(7)	0.248(1)	1.3(2)
N assisted	1	N	2.3(2)	0.192(1)	0.6(1)
	2	Fe	4.2(9)	0.260(2)	1.2(2)
	3	Fe	2.3(4)	0.278(3)	1.2(2)[a]
	4	Fe	4(1)	0.388(3)	1.2(2)[b]

[a]The Debye-Waller factor of the third shell was assumed to be equal to that of the second shell.

[b]The Debye-Waller factor of the fourth shell was assumed to be equal to that of the second shell.

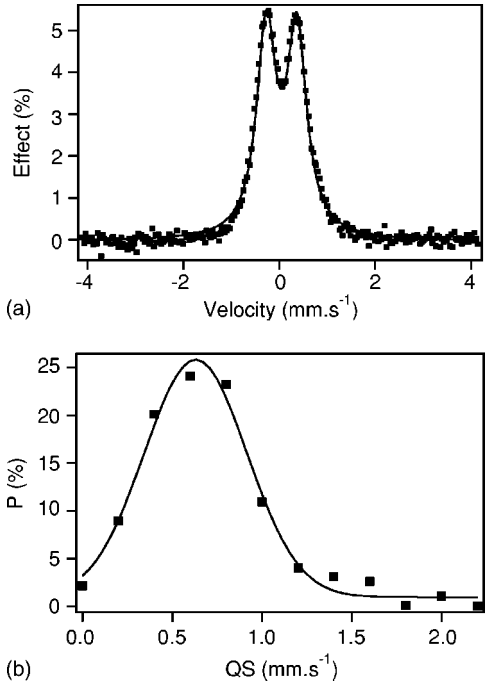

FIG. 11. (a) ^{57}Fe Mössbauer spectrum at room temperature of a Ne-assisted Fe-BN film and (b) the derived quadrupole splitting distribution. The solid line in (b) was obtained by fitting the discrete probabilities to a Gaussian curve.

CEM spectra of unassisted and Ar-, Ne-, N-assisted Fe-BN films, ~200-nm thick, have been measured and, as a typical example, the spectrum of the Ne assisted film is shown in Fig. 11(a). All spectra exhibit doublets typical of superparamagnetic relaxation, which is as expected since the $D^{\parallel}$ and $D^{\perp}$ diameters of the Fe-rich particles measured through GISAXS experiments in Sec. II B appear to be markedly lower than 10 nm in all Fe-BN films. As no magnetic splitting (or broadening) was evidenced, each spectrum was fitted to the superposition of sets of two Lorentzian lines with different quadrupole splitting (QS), thus leading to a discrete distribution of QS. Here, the width of the Lorentzian lines was assumed to be 0.26 mm/s. When the doublet structure is asymmetric, we assumed a linear relation between QS and IS to get the best fitting. The QS distribution curve obtained from the spectrum in Fig. 11(a) is presented in Fig. 11(b), where it is seen that the distribution covers the velocity range between 0 and 1.5 mm/s. The hyperfine parameters, i.e., the mean isomer shift $\langle$IS$\rangle$, the mean quadrupole

TABLE V. Summary of Mössbauer parameters as derived from quadrupole splitting (QS) distributions. ⟨IS⟩ is the mean isomer shift, ⟨QS⟩ the mean QS value, σ_{QS} the standard deviation of the QS distribution, and FWHM the full width at half maximum of the QS distribution. The experimental error bar for ⟨IS⟩ and ⟨QS⟩ is ±0.02 mm/s.

Sample	⟨IS⟩ (mm s^{-1})	⟨QS⟩ (mm s^{-1})	σ_{QS} (mm s^{-1})	FWHM (mm s^{-1})
Unassisted	0.16	0.69	0.35	0.72
N assisted	0.32	0.71	0.45	0.80
Ne assisted	0.14	0.68	0.33	0.71
Ar assisted	0.14	0.68	0.33	0.71

splitting ⟨QS⟩, and the standard deviation σ_{QS} calculated from the QS distributions are listed in Table V. Finally, all discrete QS distributions were fitted to Gaussian curves, thus allowing the FWHM of the distributions to be extracted (the derived FWHM values are also given in Table V).

CEMS results show that the hyperfine parameters for the unassisted and inert-gas assisted films are close to each other. On the contrary, the parameters for the N-assisted film markedly deviate, except for ⟨QS⟩, from the former ones, and this finding is in consistence with the above SAED and EXAFS results which already evidenced the particular role of the nitrogen assistance. An important result is the ⟨IS⟩ increase from 0.14–0.16 mm/s for the unassisted and inert-gas assisted films to 0.32 mm/s for the N-assisted film.

In the present study the most reliable hyperfine parameter is the isomer shift which is a measure of the electron density at the Fe nucleus relative to that in the standard. For the Fe nucleus, a positive isomer shift represents a decrease in electron density at the nucleus. This electron density is entirely due to the s-electrons, but it may be also modified by the shielding effects of electrons in other orbitals. In Fe-B compounds, it has been stated that the change in isomer shift is due to transfer of electrons from B to Fe atoms.[43] The variations in room-temperature isomer shift as a function of B content are plotted in Fig. 12(a) for amorphous Fe-B compounds according to Refs. 44 and 45. In the case of unassisted and inert-gas assisted films, the EXAFS data in Sec. IV B evidenced the presence of amorphous $Fe_{100-x}B_x$ nanoparticles embedded in a BN matrix. The experimental ⟨IS⟩ values at 0.14–0.16 mm/s then indicate that the Fe environments in the films under study correspond to those in $Fe_{100-x}B_x$ amorphous compounds with $x=35-37$. The Fe-rich phases detected here by analysis of the CEM spectra are in satisfactory agreement with those detected by Papaefthymiou *et al.*,[7] namely, $Fe_{60}B_{40}$ and $Fe_{80}B_{20}$, in granular Fe_{27}-$(BN)_{73}$ films prepared by rf-magnetron sputtering. Finally, let us mention that $Fe_{100-x}B_x$ amorphous alloys with $x\sim35$ are magnetically ordered at room temperature,[46] so that the appearance of a doublet as CEM spectrum from such compounds shows proof of superparamagnetic behavior for the Fe-rich particles, as already demonstrated in Ref. 8 from magnetic measurements of an unassisted film.

Similar analysis can be performed with the N-assisted film, for which SAED analysis and EXAFS measurements

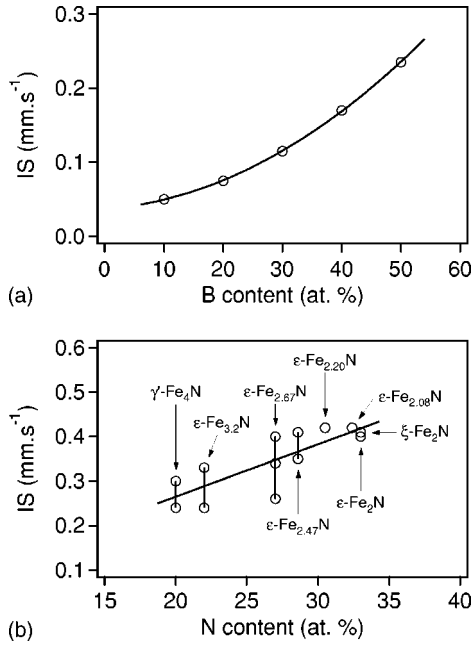

FIG. 12. (a) Variations in room temperature isomer shift as a function of B content in amorphous Fe-B compounds. Data were taken from Refs. 44 and 45. (b) Variations in room-temperature isomer shift as a function of N content in crystallized Fe-N compounds. Various symbols at the same abscissa correspond to different Fe sites in the same compound. Data were taken from Ref. 47. The solid curve was obtained by fitting the data to a straight line.

suggested the formation of crystallized ε-Fe_3N. The variations in room-temperature isomer shift as a function of N content are plotted in Fig. 12(b) for crystallized Fe_xN nitrides with $2.0\leqslant x\leqslant 4.0$.[47] It then appears that the experimental ⟨IS⟩ value at 0.32 mm/s corresponds to the 25 at. % N composition, i.e., to the ε-$Fe_{3.0}N$ nitride. The determination of this compound is consistent with the EXAFS results. In bulk Fe_xN compounds, the transition from ferromagnetic state to paramagnetic state at room temperature occurs for x close to 2.2,[47] so that the ε-$Fe_{3.0}N$ nitride is normally ferromagnetic at 293 K. Hence the observation of a Mössbauer doublet from this compound clearly indicates the existence of superparamagnetic particles.

As a conclusion, the above CEMS study brought quantitative results concerning the Fe environments in the Fe-rich particles embedded in Fe-BN nanocomposite films prepared by ion-beam sputtering. In the case of amorphous Fe-B particles, the Fe/B atomic ratio was determined to be ~2, while for Fe-N crystallized particles the Fe/N ratio is ~3.

V. SUMMARY AND CONCLUSIONS

Fe-BN nanocomposite thin films have been fabricated by ion-beam assisted sputtering codeposition with various assistance conditions. The results presented in Sec. III and IV evidence strong dependence of the structural characteristics of the films (morphology and organization of the nanoparticles as well as local chemical order) on the nature of the

assistance beam. The first interesting feature revealed by cross-section HRTEM observations and confirmed quantitatively by GISAXS experiments is the synthesis of more or less columnar nanoparticles when the codeposition is assisted, whether the assistance beam is reactive or not. Such a columnar growth can be attributed to an enhanced surface diffusion of the incoming deposited species, which could be also responsible for an increase of the in-plane diameter.[8,24] However, as seen in Table III, this effect is limited when nitrogen is used because N reacts with Fe to form crystallized ε-Fe_3N nanoparticles and with B to form *h*-BN nanocapsules. In contrast, nanoparticles obtained in inert-gas assisted and unassisted films are in the form of a Fe_2B amorphous phase. The presence of B atoms dissolved in the nanoparticles can be simply explained by an excess of B atoms in the matrix (B:N ratio higher than 1) and also by the formation energy of the Fe-B bonds which is negative and smaller than that of the Fe-N bonds over the whole concentration range.[48] The second striking result is that, in correlation with the columnar growth, self-ordering of the nanoparticles and narrowing of the size distribution are clearly evidenced in inert-gas-assisted films by TEM image processing as well as by GISAXS pattern analysis. Regarding the nanostructural characteristics of the Fe-BN nanocomposite films assisted with different inert gas, slight variations are observed (Table III). It is, however, worth noting that efficiency of the assistance to induce columnar growth and self-ordering is actually maximized in the argon assistance case. This result suggests that when neon and krypton are used, part of the ions in the assistance beam do not transfer their energy to the surface atoms of the growing film, most probably due to backscattering and sputtering effects. Indeed, a large amount of Ne ions are backscattered (10.9% compared to 4.7% for Ar and 0.3% for Kr, as determined from SRIM calculations[49]), while sputtering arises when krypton is used, as described in Sec. II.

To conclude, we have synthesized self-organized arrays of Fe-rich nanoparticles encapsulated in *h*-BN and characterized by a high shape anisotropy and a small size dispersion. Furthermore, depending on the nature of the assistance gas, we have obtained nanoparticles with various compositions and crystalline structures, from amorphous borides to crystallized nitrides. However, the Fe-rich nanoparticles described here are superparamagnetic at room temperature whereas ferromagnetic phases should be stabilized for developing new materials for high-density magnetic recording media. In the future, one can expect to control the composition of the nanoparticles independently of their shape and organization by using mixed gas (e.g., Ar+N with variable Ar:N ratios). Hence, the results obtained here provide motivation to extend the fabrication method to nanoparticles of ferromagnetic alloys with large magnetocrystalline anisotropies (e.g., FePt and CoPt) or with large saturation magnetization (e.g., $Fe_{16}N_2$ for which a giant moment has been reported).[50]

ACKNOWLEDGMENTS

We acknowledge the assistance of the LURE-DCI technical staff during the GISAXS and EXAFS experiments. We thank A. Traverse for his contribution to EXAFS experiments. E. Fonda has been fully supported during this research by the E. U. program "Human Potential" (Contract No. HPMF-CT-20001-01125).

APPENDIX A

The GISAXS intensity originating from particles with in-plane diameter D and height H was fitted with the following expressions for the form factor:

$$F_{\text{cylinder}}(\tilde{q_y},\tilde{q_z}) = \frac{\pi}{2}D^2H\frac{J_1\left(\tilde{q_y}\frac{D}{2}\right)}{\tilde{q_y}\frac{D}{2}}\frac{\sin\left(\tilde{q_z}\frac{H}{2}\right)}{\tilde{q_z}\frac{H}{2}}, \tag{A1}$$

$$F_{\text{spheroid}}(\tilde{q_y},\tilde{q_z}) = \int_0^{H/2}\pi D^2\left(1-4\frac{z^2}{H^2}\right) \times\frac{J_1\left(\tilde{q_y}\frac{D}{2}\sqrt{1-4\frac{z^2}{H^2}}\right)}{\tilde{q_y}\frac{D}{2}\sqrt{1-4\frac{z^2}{H^2}}}\cos(\tilde{q_z}z)dz, \tag{A2}$$

$$F_{\text{capsule}}(\tilde{q_y},\tilde{q_z}) = \frac{\pi}{2}D^2(H-D)\frac{J_1\left(\tilde{q_y}\frac{D}{2}\right)}{\tilde{q_y}\frac{D}{2}}\frac{\sin\left(\tilde{q_z}\frac{H-D}{2}\right)}{\tilde{q_z}\frac{H-D}{2}} + \int_0^{D/2}\pi(D^2-4z^2) \times\frac{J_1\left(\tilde{q_y}\sqrt{\frac{D^2}{4}-z^2}\right)}{\tilde{q_y}\sqrt{\frac{D^2}{4}-z^2}} \times\cos\left[\tilde{q_z}\left(z+\frac{H-D}{2}\right)\right]dz. \tag{A3}$$

APPENDIX B

The structure factor for monodisperse hard-spheres with diameter D_{HS} and volume fraction η_{HS}, describing the interference effects, was expressed as[26]

$$S(\tilde{q}) = [1+24\eta_{\text{HS}}G(D_{\text{HS}}\tilde{q})/(D_{\text{HS}}\tilde{q})]^{-1}, \tag{B1}$$

where

$$G(A) = \alpha(\sin A - A\cos A)/A^2 + \beta[2A\sin A + (2 - A^2)\cos A - 2]/A^3 \quad \text{(B2)}$$

$$+ \gamma\{-A^4\cos A + 4[(3A^2 - 6)\cos A + (A^3 - 6A)\sin A + 6]\}/A^5 \quad \text{(B3)}$$

and

$$\alpha = (1 + 2\eta_{HS})^2/(1 - \eta_{HS})^4, \quad \text{(B4)}$$

$$\beta = -6\eta_{HS}(1 + \eta_{HS}/2)^2/(1 - \eta_{HS})^4, \quad \text{(B5)}$$

$$\gamma = \eta_{HS}\alpha/2. \quad \text{(B6)}$$

*Electronic address: david.babonneau@univ-poitiers.fr
†Present address: Synchrotron SOLEIL, L'Orme des Merisiers, Saint-Aubin, BP 48, 91192 Gifsur-Yvette Cedex, France

[1] G. Xiao and C. L. Chien, Appl. Phys. Lett. **51**, 1280 (1987); S. H. Liou and C. L. Chien, *ibid.* **52**, 512 (1988).
[2] C. Chen, O. Kitakami, and Y. Shimada, J. Appl. Phys. **84**, 2184 (1998).
[3] N. M. Dempsey, L. Ranno, D. Givord, J. Gonzalo, R. Serna, G. T. Fei, A. K. Petford-Long, R. C. Doole, and D. E. Hole, J. Appl. Phys. **90**, 6268 (2001).
[4] D. Kumar, J. Narayan, A. V. Kvit, A. K. Sharma, and J. Sankar, J. Magn. Magn. Mater. **232**, 161 (2001).
[5] H. Karamon, T. Masumoto, and Y. Makino, J. Appl. Phys. **57**, 3527 (1985).
[6] A. S. Edelstein, B. N. Das, R. L. Holtz, N. C. Koon, M. Rubistein, S. A. Wolf, and K. E. Kilstrom, J. Appl. Phys. **61**, 3320 (1987).
[7] V. Papaefthymiou, A. Tsoukatos, G. C. Hadjipanayis, A. Simopoulos, and A. Kosticas, J. Magn. Magn. Mater. **140-144**, 397 (1995); G. C. Hadjipanayis, A. Tsoukatos, V. Papaefthymiou, A. Simopoulos, and A. Kosticas, Scr. Metall. Mater. **33**, 1679 (1995).
[8] D. Babonneau, M. Jaouen, M.-F. Denanot, P. Guérin, and F. Petroff, Appl. Phys. Lett. **82**, 3056 (2003).
[9] D. Babonneau, T. Cabioc'h, M.-F. Denanot, and A. Naudon, Appl. Phys. Lett. **74**, 800 (1999).
[10] D. Babonneau, J. Briatico, F. Petroff, T. Cabioc'h, and A. Naudon, J. Appl. Phys. **87**, 3432 (2000).
[11] T. Hayashi, S. Hirono, M. Tomita, and S. Umemura, Nature (London) **381**, 772 (1996).
[12] J.-J. Delaunay, T. Hayashi, M. Tomita, S. Hirono, and S. Umemura, Appl. Phys. Lett. **71**, 3427 (1997).
[13] O. Mamezaki, H. Adachi, S. Tomita, M. Fujii, and S. Hayashi, Jpn. J. Appl. Phys., Part 1 **39**, 6680 (2000).
[14] J. A. Christodoulides, M. J. Bonder, Y. Huang, Y. Zhang, S. Stoyanov, G. C. Hadjipanayis, A. Simopoulos, and D. Weller, Phys. Rev. B **68**, 054428 (2003).
[15] T. Hirano, T. Oku, and K. Suganuma, J. Mater. Chem. **9**, 855 (1999).
[16] M. Kuno, T. Oku, and K. Suganuma, Scr. Mater. **44**, 1583 (2001).
[17] J. A. Christodoulides, Y. Huang, Y. Zhang, G. C. Hadjipanayis, I. Panagiotopoulos, and D. Niarchos, J. Appl. Phys. **87**, 6938 (2000).
[18] M. Daniil, P. A. Farber, H. Okumura, G. C. Hadjipanayis, and D. Weller, J. Magn. Magn. Mater. **246**, 297 (2002).
[19] G. Y. Fan and J. M. Cowley, Ultramicroscopy **17**, 345 (1985).
[20] J. Neter, W. Wasserman, and G. A. Whitmore, *Applied Statistics*, 3rd ed. (Allyn and Bacon, Newton, MA, 1988).
[21] P. Favia, T. Stoto, M. Carrad, P. A. Stadelmann, and L. Zuppiroli, Microsc. Microanal. Microstruct. **7**, 225 (1996).
[22] J. H. We, W. W. Wu, H. H. Lin, S. L. Cheng, Y. L. Chueh, L. J. Chou, and L. J. Chen, Appl. Surf. Sci. **212-213**, 325 (2003).
[23] M. Rauscher, R. Paniago, H. Metzger, Z. Kovats, J. Domke, J. Peisl, H. D. Pfannes, J. Schulze, and I. Eisele, J. Appl. Phys. **86**, 6763 (1999).
[24] D. Babonneau, S. Camelio, T. Girardeau, M. Jaouen, and O. Lyon, J. Appl. Crystallogr. **36**, 430 (2003).
[25] M. Rauscher, T. Salditt, and H. Spohn, Phys. Rev. B **52**, 16 855 (1995).
[26] J. S. Pedersen, J. Appl. Crystallogr. **27**, 595 (1994).
[27] D. Babonneau, I. R. Videnović, M. G. Garnier, and P. Oelhafen, Phys. Rev. B **63**, 195401 (2001).
[28] E. Cattaruzza, F. d'Acapito, F. Gonella, A. Longo, A. Martorana, G. Mattei, C. Maurizio, and D. Thiaudière, J. Appl. Crystallogr. **33**, 740 (2000).
[29] N. W. Ashcroft and J. Lekner, Phys. Rev. **145**, 83 (1966).
[30] R. Triolo, E. Caponetti, and S. Spooner, Phys. Rev. B **39**, 4588 (1989).
[31] W. H. Press, B. P. Flannery, S. A. Teukolski, and W. T. Vetterling, *Numerical Recipes in C*, 2nd ed. (Cambridge University Press, New York, 1992).
[32] Joint Committee on Powder Diffraction Standards, 2000. JCPDS-ICDD Powder Diffraction Database, cards No. 6-696, 73-2101, 73-2102, 36-1332, 34-421. Swarthmore, Pennsylvania, USA.
[33] G. Tourillon, E. Dartyge, A. Fontaine, M. Lemonnier, and F. Bartol, Phys. Lett. A **121**, 251 (1987).
[34] O. Proux, J. Mimault, and T. Girardeau, Philos. Mag. A **81**, 2199 (2001).
[35] S. S. L. Schroeder, Solid State Commun. **98**, 405 (1996).
[36] T. Guo and M. L. denBoer, Phys. Rev. B **31**, 6233 (1985).
[37] T. Girardeau, J. Mimault, M. Jaouen, P. Chartier, and G. Tourillon, Phys. Rev. B **46**, 7144 (1992).
[38] M. Newville, P. Livins, Y. Yacoby, J. J. Rehr, and E. A. Stern, Phys. Rev. B **47**, 14 126 (1993).
[39] M. Newville, B. Ravel, D. Haskel, J. J. Rehr, E. A. Stern, and Y. Yacoby, Physica B **208–209**, 154 (1995).
[40] A. L. Ankudinov, B. Ravel, J. J. Rehr, and S. D. Conradson, Phys. Rev. B **58**, 7565 (1998); A. L. Ankudinov and J. J. Rehr, *ibid.* **62**, 2437 (2000).
[41] D. Bodin and J.-P. Eymery, Nucl. Instrum. Methods Phys. Res. B **16**, 424 (1986).
[42] D. Liljequist, T. Ekdahl, and U. Baverstam, Nucl. Instrum. Methods **155**, 529 (1978).
[43] J. D. Cooper, T. C. Gibb, N. N. Greenwood, and R. V. Parish,

Trans. Faraday Soc. **60**, 2097 (1964).
[44] H. Komatsu, N. Kataoka, K. Fukamichi, and T. Goto, Nucl. Instrum. Methods Phys. Res. B **76**, 89 (1993).
[45] G. Xiao and C. L. Chien, Phys. Rev. B **35**, 8763 (1987).
[46] C. L. Chien, D. Musser, E. M. Gyorgy, R. C. Sherwood, H. S. Chen, F. E. Luborsky, and J. L. Walter, Phys. Rev. B **20**, 283 (1979).
[47] G. M. Chen, N. K. Jaggl, J. B. Butt, E. B. Yeh, and L. H. Schwartz, J. Phys. Chem. **87**, 5326 (1983).
[48] *Smithells Metals Reference Book*, 7th ed., edited by E. A. Brandes and G. B. Brook (Butterworth-Heinemann, Oxford, 1992).
[49] J. F. Ziegler and J. P. Biersak, http://www.srim.org/
[50] J. Q. Xiao and C. L. Chien, Appl. Phys. Lett. **64**, 384 (1994).